
Fast 4D Mesh Generation by Spatio-Temporal Attention Chains

Dvir Samuel¹ Yuval Atzmon¹ Gal Chechik^{1,2} Yoni Kasten¹
¹NVIDIA Research, Tel-Aviv, Israel
²Bar-Ilan University, Ramat-Gan, Israel

Abstract

4D mesh generation has recently emerged as a powerful paradigm for recovering dynamic 3D structure from videos, but existing methods remain slow, computationally expensive, and difficult to scale to longer sequences. We introduce a training-free approach that accelerates 4D mesh generation while improving temporal correspondence quality. Our key observation is that temporal correspondences emerge inside a 4D backbone long before its generated meshes become visually accurate. We exploit this with a general framework we call Spatio-Temporal Attention Chain which propagates information across space and time. Starting from vertices on an anchor mesh, the chain maps vertices to latent tokens. It then follows temporal correspondences in latent space, and recovers frame-specific vertices through latent-to-vertex attention. This design avoids expensive explicit matching while preserving anchor mesh details and thereby improving dynamic mesh geometry and temporal consistency.

Compared to state-of-the-art, our method generates a 4D mesh in 9 seconds, achieving a $13\times$ speedup while producing higher-quality results. Moreover, our approach scales to videos up to $16\times$ longer without degrading mesh quality. Beyond generation, the improved correspondences enable competitive zero-shot performance on two downstream tasks: 2D object tracking and 4D tracking. We further show that our framework enables reliable camera estimation, a capability not supported by prior 4D mesh generation methods. [Project Page](#)

1 Introduction

Understanding a dynamic 3D world is a central goal of computer vision, and a foundation for embodied AI, physical reasoning, simulation, and virtual reality. Yet progress on dynamic 3D lags far behind images and videos. The bottleneck is data scarcity: high-quality 4D data must capture both 3D structure and motion over time, making it rare and expensive to acquire. This motivates recovering 4D from ordinary videos, a far more scalable source of motion and shape [26, 56, 91, 85, 79]. In this work, we focus on *video-to-dynamic-mesh reconstruction*: recovering a temporally coherent 3D mesh sequence from a video of a moving object.

Reconstructing dynamic geometry from monocular video is challenging because the model must infer detailed 3D geometry in every frame while preserving surface identity across time, a requirement that is hard to learn under scarce 4D supervision [8, 42, 58, 90, 59]. ActionMesh [59] resolves this with a staged design. A 4D generative diffusion backbone first lifts the video into 3D latents with frame-specific topology; a separate network then animates an anchor mesh to enforce shared connectivity. While effective, this design is costly. The generative stage requires significant time to produce high-quality geometry; the second stage adds non-end-to-end training; and the full pipeline remains tied to scarce 4D supervision. Beyond these costs, the output mesh lies in an arbitrary coordinate frame with no link back to input pixels, preventing downstream applications like 4D and

2D tracking, camera recovery, or scene composition [14, 31, 84, 33, 74]. Finally, training on short clips makes this drift or collapse on longer videos.

That additional stage nevertheless reveals an important fact: the geometry comes from a simpler image-to-3D anchor, while the heavy 4D generative backbone contributes only a 4D motion prior. This raises a natural question: how can we apply that prior directly to the anchor, without a separate neural animator?

We show that the answer lies inside the 4D generative backbone itself: our key observation is that useful temporal correspondences already emerge when we run denoising with as few as four denoising steps, where attention patterns already link anchor-frame 3D tokens to matching tokens in later frames. We expose this signal through a *Spatio-Temporal Attention Chain*. At a high level, the chain treats *attention as a soft Markov transport*: each attention row is a probability distribution over latent tokens, so multiplying attention maps gives the probability of moving from one representation to the next. Concretely, it links an anchor-frame vertex to an anchor-frame latent token ($V_a \rightarrow Z_a$), transports it across time to frame f via temporal self-attention ($Z_a \rightarrow Z_f$), and projects it back to a 3D point in the target frame ($Z_f \rightarrow V_f$).

This shifts the role of the backbone: instead of producing a high-resolution mesh per frame with 30 denoising steps, we run the denoiser with four steps and read the correspondence field it already computes. By tracking sparse landmarks through the chain and lifting them to the anchor mesh via geodesic-rigid skinning, we drop the second stage entirely. Generation time therefore falls from nearly two minutes to roughly nine seconds, preserving topology by construction and improving 3D accuracy. Beyond speed, the chain naturally connects 2D patches, latent tokens, and mesh vertices, unlocking three additional capabilities. First, when extending generation from 16 to 240 frames autoregressively, reinforcing the strongest correspondences during denoising substantially reduces geometric drift without retraining. Second, different chain compositions yield competitive zero-shot 3D point trajectories (4D tracking) and 2D point trajectories. Third, the resulting 2D-to-3D matches allow recovering per-frame cameras, placing the mesh back into a reconstructed scene (Fig. 4).

Contributions. (1) We identify spatio-temporal attention chains as a hidden correspondence signal linking pixels, latent tokens, and mesh vertices inside a 4D generative backbone. (2) We propose a training-free framework for 4D generative backbones that tracks sparse landmarks through these chains and lifts them to a full animated mesh, cutting inference from 120s to 9s at favorable quality. (3) We improve autoregressive generation by reinforcing these correspondences to reduce drift, enabling coherent $16\times$ longer sequences. (4) We show that the same chains yield several capabilities missing in prior work: competitive zero-shot 4D and 2D point tracking, as well as camera recovery from 2D-3D matches.

2 Related Work

Image-to-3D generative backbones. Our chain reads attention weights off a VecSet-style 3D decoder [95], which reconstructs geometry by cross-attending 3D query points to a compact set of latent tokens encoding the shape. We instantiate on TripoSG [41], a flow-based image-to-3D generator producing high-fidelity meshes from a single image. The same decoder structure underlies CLAY [99], Craftsman [38], Dora-VAE [9], and Hunyuan3D [70], and our chain could be adapted to other generators sharing this structure. Other representation classes include Trellis’s [82] sparse structured latents (SLAT) based on active voxels, LRM’s [23] triplanes, LGM’s [68] Gaussian primitives, and AssetGen’s [63] PBR-textured meshes.

Video-to-4D generation. Per-scene optimization pipelines [26, 56, 91, 80, 93, 78, 97, 44] distill dynamic 3D from video using diffusion priors, taking minutes to hours per clip. Multi-view video diffusion [85, 88, 79, 25] generates feed-forward novel-view sequences but still needs per-scene optimization for 4D. Feed-forward 4D methods predict spatial primitives directly, typically in topology-free spaces: L4GM [57] and 4DGT [87] produce Gaussian sequences, Motion2VecSets [6] denoises vector sets, and ShapeGen4D [90] adds temporal attention to a 3D generator; all decode frames independently, lacking shared topology. Prior methods therefore add an explicit topology stage: ActionMesh [59] learns a temporal 3D autoencoder that deforms a reference mesh via per-frame anchor displacements, $\mathbf{V}_f = \mathbf{V}_a + \Delta_f$, while optimization-based methods [8, 42, 58] impose topology or temporal consistency through registration, deformation, or optimized implicit representations. In contrast, our approach extracts dense correspondences directly from the temporal

backbone, bypassing any separate topology-enforcing or animation stage. A related line animates a given mesh via predicted skeletons [19, 64, 46, 89] or deformation fields [50, 61, 81]; these methods assume clean input assets and predict explicit skeletons and skinning weights.

Emergent Correspondences in Diffusion Features: Two recent lines tap frozen diffusion models for zero-shot correspondence. One matches features as descriptors: DIFT [69] on UNet activations, Diff3F [15] lifting them onto 3D shapes, MbQ [2] on video-DiT queries for Q-injection, and Track4Gen [24] via an auxiliary tracking loss. The other reads attention weights directly: CAMEO [34] in multi-view 3D attention, DiTFlow [53] as a per-clip optimization loss, and DiffTrack [51] on video-DiT temporal-matching layers; Point Prompting [62] sidesteps both via counterfactual prompting. We instead *compose* three attention maps of a frozen 4D generator – vertex-to-token, temporal token-to-token, and token-to-surface – into a $V_a \rightarrow Z_a \rightarrow Z_f \rightarrow V_f$ chain yielding correspondences tied to an anchor mesh’s surface through a forward pass – no optimization, no external tracker.

Attention Control in Diffusion Models: A complementary line manipulates or analyzes frozen attention. Several methods reweight cross/self-attention [22, 60] for editing, inject self-attention features [73] for structure, or share self-attention across images [5, 72] for identity; TiARA [40] suppresses temporal attention weights for extended video generation. A related thread treats attention rows as probability distributions and composes them to trace information flow within a single transformer [1, 7, 16]. Building on this view, we compose attention across separately-trained modules and modalities of a 4D pipeline – vertex-to-token, token-to-token, token-to-surface – and reinforce reliable matches to stabilize long sequences.

Point tracking and monocular 4D geometry. Our method outputs 2D and 3D point trajectories. Supervised 2D trackers [20, 14, 13, 31, 29, 11, 36, 21] are driven by standard benchmarks [12, 101]; 3D trackers [84, 83, 94] update point clouds, while 4RC [49], Trace-Anything [47], and TracksTo4D [33] predict motion fields and MegaSaM [43] runs deep visual SLAM. A separate line predicts metric pointmaps, introduced by DUS3R [77] and extended for dynamic scenes [28, 17, 98, 76, 86]; closest in spirit, Easi3R [10] achieves 4D reconstruction via training-free attention adaptation of DUS3R. These methods either require per-frame mesh reconstruction from scattered points or depend on pointmap supervision. In contrast, our approach requires no tracker or pointmap supervision. Furthermore, our single forward pass directly outputs the skinned mesh alongside the 2D-3D matches needed for PnP+RANSAC [37, 4] camera pose estimation.

3 4D Mesh Generation: Preliminaries and Notations

Video-to-dynamic-mesh methods map a video of F frames, to a temporally coherent 4D mesh sequence $\mathcal{M}_{1:F} = \{(\mathbf{V}_f, \mathcal{F})\}_{f=1}^F$, where \mathcal{F} and $\mathbf{V}_f \in \mathbb{R}^{|V| \times 3}$ define a fixed topology and shared vertex identities across time.

We denote attention between a query sequence \mathbf{X} and context sequence \mathbf{Y} by:

$$A_{\mathbf{X} \rightarrow \mathbf{Y}} = \text{softmax}((\mathbf{X}\mathbf{W}_Q)(\mathbf{Y}\mathbf{W}_K)^T / \sqrt{d_k}), \quad \text{Attn}(\mathbf{X}, \mathbf{Y}) = A_{\mathbf{X} \rightarrow \mathbf{Y}} \cdot (\mathbf{Y}\mathbf{W}_V) \quad (1)$$

where \mathbf{W}_Q , \mathbf{W}_K , and \mathbf{W}_V project inputs to queries, keys, and values.

Recent pipelines [59, 8, 27] employ a three-staged approach: (0) an image-to-3D model reconstructs initial reference geometry, (I) temporal or independent generators produce per-frame 3D representations, and (II) a final topology-preserving stage aligns the vertices through time so all frames share the same connectivity.

Stage 0: Image-to-3D anchor reconstruction. An image-to-3D denoiser model (e.g. [41]) reconstructs an anchor mesh $\mathcal{M}_a = (\mathbf{V}_a, \mathcal{F})$ with shape latent $\mathbf{z}_a \in \mathbb{R}^{N \times d}$ composed of N tokens of dimension d . Then, a VAE’s transformer decoder expresses each anchor vertex as an attention-weighted combination of latent tokens, yielding $A_{V_a \rightarrow Z_a} \in \mathbb{R}^{|V_a| \times N}$. Image cross-attention similarly links anchor image patches P_a to the same tokens, giving $A_{P_a \rightarrow Z_a}$.

Stage I: Video-to-4D mesh generation. Given the anchor latent \mathbf{z}_a and the input video, a temporal denoiser Φ_θ predicts one latent \mathbf{z}_f for each frame f . Inflated self-attention inside Φ_θ links tokens in \mathbf{z}_a to tokens in \mathbf{z}_f , giving $A_{Z_a \rightarrow Z_f} \in \mathbb{R}^{N \times N}$.

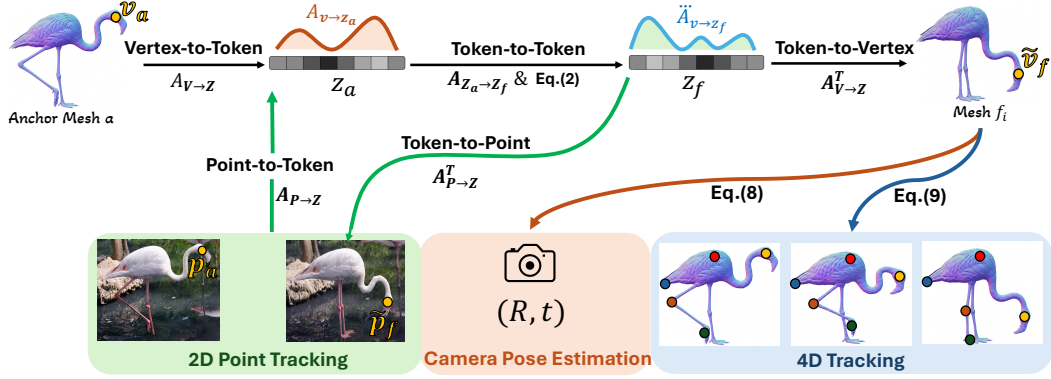


Figure 1: **Method overview.** Our attention chain follows a point through the frozen 4D generator: from an anchor mesh vertex to latent tokens, across time to target-frame tokens, and back to a target mesh vertex. Image-patch endpoints give analogous chains for 2D tracking, camera pose estimation, and 4D tracking, without additional training.

Stage II: Topology-consistent decoding. To maintain consistent topology, prior pipelines add a topology-preserving stage to predict per-frame displacements using learned decoders [27, 59] or test-time optimization [8, 42]. In contrast, we drop this stage, recovering anchor motion directly from attention-chain correspondences.

4 Method

Current staged pipelines [59, 8] treat geometry generation and animation as separate tasks. However, relying on a dedicated Stage II requires an entirely separate network, adding significant computational overhead during both training and inference. Moreover, these pipelines typically remain restricted to short, drift-prone temporal windows (Fig. 2). We aim to accelerate and scale topology-preserving 4D generation without any additional training. Our core observation is that a frozen pipeline like ActionMesh [59] inherently encodes temporal tracking within its features. Instead of relying on a learned decoder, we extract 3D correspondences directly during the denoising process (stages 0 and I) via an *attention chain*. Conceptually, each attention matrix is a soft transition map, and multiplying them transports probability mass from anchor vertices, through latent tokens, to target surface points. This chain maps anchor vertices (V_a) to latent tokens (Z_a), transports them across frames via temporal self-attention ($Z_a \rightarrow Z_f$), and projects them back to target surface points V_f at frame f :

$$V_a \rightarrow Z_a \rightarrow Z_f \rightarrow V_f$$

These correspondences emerge within just a few denoising steps. We then animate the anchor mesh using a fast closed-form deformation model. By strictly reusing the constant face set \mathcal{F} , we guarantee perfect topology consistency by construction.

4.1 Correspondence from the Attention Chain

For each anchor vertex v and target frame f , we seek a target surface point \tilde{v}_f . Instead of training a separate deformation network, we establish tracking with an attention chain (Fig. 1). The chain links the anchor and target geometries through intermediate representations by sequentially multiplying the backbone’s internal spatial and temporal attention maps. This composes localized attention steps into a dense correspondence map. We assemble the chain from three components.

(1) Vertex-to-token attention ($V_a \rightarrow Z_a$). During Stage 0 (Sec. 3), the 3D decoder yields the cross-attention matrix $A_{V_a \rightarrow Z_a} \in \mathbb{R}^{|V_a| \times N}$. Since the softmax normalization is applied over the latent key dimension, each row $A_{V_a \rightarrow Z_a}[v, :]$ forms a valid probability distribution. This row explicitly describes which latent tokens explain anchor vertex v , where each entry represents the probability that anchor token t relates to that specific vertex.

(2) Token-to-token temporal attention ($Z_a \rightarrow Z_f$). During the denoising step of Stage I, the inflated temporal self-attention layers process all frames simultaneously. For a given target frame f , we extract

the attention weights linking anchor-frame tokens to frame- f tokens to yield $A_{Z_a \rightarrow Z_f} \in \mathbb{R}^{N \times N}$. This matrix governs the transfer of structural information from the anchor frame to the target frame at the latent token level.

(3) Token-to-surface attention ($Z_f \rightarrow V_f$). For target frame f , the 3D decoder turns Z_f into an implicit field. We extract candidate surface points $S_f = \{x_u^{(f)}\}_{u=1}^{|V_f|}$ from this field and query them against the frame- f latent tokens. The resulting cross-attention matrix $A_{Z_f \rightarrow V_f}^T \in \mathbb{R}^{|V_f| \times N}$ relates each candidate surface point u to these tokens.

Composing the attention chain. We compose the attention matrices above to map anchor vertex v to frame f . The row $A_{V_a \rightarrow Z_a}[v, :]$ gives weights over anchor tokens. Multiplying this row by $A_{Z_a \rightarrow Z_f}$ transfers those weights to frame- f tokens $t' \in Z_f$:

$$\ddot{A}_{v, Z_f}(t') = \sum_{t=1}^N A_{V_a \rightarrow Z_a}[v, t] A_{Z_a \rightarrow Z_f}[t, t'], \quad (2)$$

where t indexes anchor-frame tokens and t' indexes tokens in frame f . The vector \ddot{A}_{v, Z_f} is therefore a probability distribution over frame- f tokens. A candidate surface point $x_u^{(f)} \in S_f$ is likely to match v when its token-level attention agrees with \ddot{A}_{v, Z_f} , so we score it by their inner product:

$$s_{v, f}(u) = \sum_{t'=1}^N \ddot{A}_{v, Z_f}(t') A_{Z_f \rightarrow V_f}^T[u, t']. \quad (3)$$

Finally, we obtain the correspondence \tilde{v}_f as a sharp softmax blend over the top-scoring surface points:

$$\tilde{v}_f = \sum_{u \in \mathcal{N}_{v, f}} \pi_{v, f}(u) x_u^{(f)}, \quad \pi_{v, f}(u) = \frac{\exp(s_{v, f}(u)/\tau)}{\sum_{q \in \mathcal{N}_{v, f}} \exp(s_{v, f}(q)/\tau)}. \quad (4)$$

Here $\mathcal{N}_{v, f}$ denotes the localized subset of top-scoring surface points and τ is a temperature hyperparameter. We also define a confidence score $c_v^{(f)} = \max_u s_{v, f}(u)$ to be used later for mesh animation.

This construction has two key properties. First, both endpoint attentions come from the same 3D decoder, so anchor vertices and target surface points are compared in a shared token–geometry space. Second, \tilde{v}_f is computed only from the top-scoring surface samples $\mathcal{N}_{v, f}$, keeping the correspondence on the target surface and reducing drift to unrelated regions.

The next step lifts these sparse correspondences to a full animated mesh while preserving the anchor topology efficiently and without any additional model training.

4.2 Topology-Preserving Animation

In early experiments, we observed that directly querying all anchor vertices and simply mapping them to their target positions using our dense correspondences produced noisy results. Instead, we obtain topology-preserving animation by tracking a sparse set of control landmarks and lifting their motion to the full mesh in three steps:

1. Landmark Extraction and Filtering: We sample a sparse set of K control landmarks on the anchor mesh by farthest point sampling. We extract their trajectories across frames via the attention chain, assigning confidence scores and rejecting physically implausible displacements as outliers.

2. Temporal Smoothing: To ensure fluid motion, we apply a confidence-weighted 1D Gaussian temporal smoothing to each landmark’s trajectory independently. This bridges gaps caused by outlier removal by interpolating each landmark from nearby reliable frames.

3. Mesh Deformation: Finally, we propagate the smoothed landmark motions to the dense mesh using Geodesic Rigid Skinning [67]. For each vertex, we compute a local rigid transformation (rotation and translation) from its closest landmarks under geodesic distance, which is measured along the mesh surface. This prevents motion from leaking between spatially close but disconnected parts, such as an arm and torso, while the local-rigid transform preserves volume and avoids the shrinkage artifacts often caused by linear blend skinning. This pipeline yields a temporally coherent animated mesh $\hat{\mathcal{M}}_f = (\hat{V}_f, \mathcal{F}_a)$ that strictly maintains the anchor topology. Full details of temporal smoothing and the weighted Procrustes skinning formulation are deferred to Appendix D.

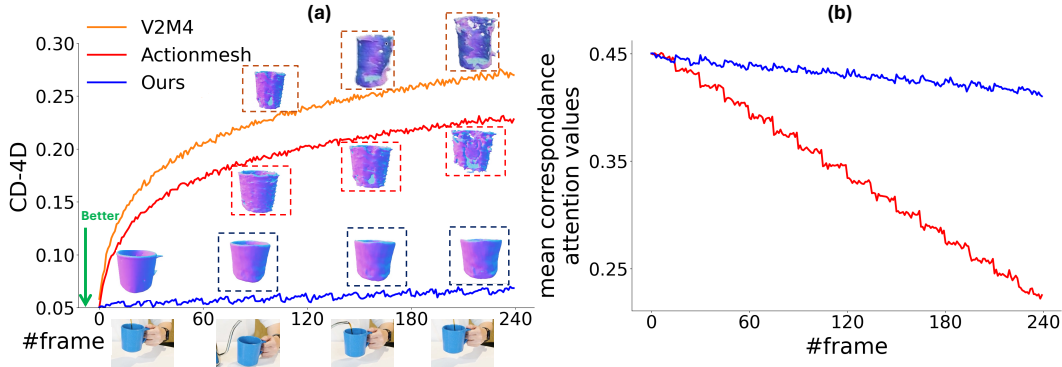


Figure 2: **Long-sequence rollout.** (a) Naive autoregressive 4D generation accumulates errors over time, degrading mesh quality. We find that this drift is driven by weakening latent correspondences across windows. (b) Our correspondence reinforcement preserves these correlations, stabilizing the rollout and maintaining high-quality generation.

4.3 Scaling to Longer Sequences

Existing 4D generators are trained on short clips, so autoregressive rollout to longer videos quickly drifts: each new window is initialized from the final latent of the previous one, and errors accumulate (Fig. 2a). We measure this on long ActionBench [59] sequences (Appendix C) and observe both degrading mesh quality (Fig. 2a) and a steady drop in the correlation of matched latent points across windows (Fig. 2b).

To prevent this drift, we reinforce temporal correspondences during denoising inside each 16-frame window. The first two denoising steps run normally, establishing initial correspondences and confidence scores $c_v^{(f)}$. During the two remaining steps, we trace the attention paths backward to identify the main latent token pair (t, t') behind each match, collect these pairs in \mathcal{C} , and scale the corresponding entries in $A_{Z_a \rightarrow Z_f}$ by their confidence:

$$\tilde{A}_{Z_a \rightarrow Z_f}[t, t'] = \frac{c_v^{(f)} A_{Z_a \rightarrow Z_f}[t, t']}{\sum_k c_v^{(f)} A_{Z_a \rightarrow Z_f}[t, k]}, \quad \forall (t, t') \in \mathcal{C}. \quad (5)$$

After these reinforced denoising steps, we use the final frame as the anchor for the next window. Boosting reliable attention paths stabilizes latent correlations and mesh quality over long sequences.

4.4 Extension to 2D and 4D Point Tracking

Beyond mesh animation, attention chaining provides a general composition mechanism: any two attention maps that share an intermediate representation can be linked, e.g., image patches to tokens, tokens to tokens, and tokens to vertices. We demonstrate this flexibility on two tasks: 2D point tracking in the input video, and 4D point tracking that recovers world-coordinate 3D trajectories for every visible pixel.

2D point tracking ($P_a \rightarrow Z_a \rightarrow Z_f \rightarrow P_f$). We replace the 3D decoder attention with the denoiser cross-attention between latent tokens and image patches. Let $A_{P_f \rightarrow Z_f} \in \mathbb{R}^{P \times N}$ denote the attention from P image patches to N latent tokens in frame f . Given a query patch p_a in the anchor frame, we transport its attention through the temporal block to find its correspondence \tilde{p}_f in frame f :

$$\tilde{p}_f = \arg \max_p \sum_{t, t'=1}^N A_{P_a \rightarrow Z_a}^T[t, p_a] A_{Z_a \rightarrow Z_f}[t, t'] A_{P_f \rightarrow Z_f}^T[t', p] \quad (6)$$

This directly reuses the temporal attention from Section 4.1 to establish semantic persistence across the video sequence without any additional computation.

2D to 3D bridge ($P \leftrightarrow V$). By composing anchor-frame attentions, we directly link image patches and mesh vertices. Notably, ActionMesh [59] lacks this capability, leaving no direct way to map

their output mesh back to the source image. In contrast, for a given anchor patch p_a or vertex v_a , we establish the following mappings :

$$\tilde{v}_p = \arg \max_v \sum_{t=1}^N A_{P_a \rightarrow Z_a}[p_a, t] A_{Z_a \rightarrow V_a}[t, v], \quad \tilde{p}_v = \arg \max_p \sum_{t=1}^N A_{P_a \rightarrow Z_a}[p, t] A_{Z_a \rightarrow V_a}[t, v_a] \quad (7)$$

This creates a training-free correspondence layer connecting the input pixels to the canonical mesh geometry.

Camera pose estimation. Using this bridge, we collect 2D to 3D correspondences $\{(\mathbf{u}_v, \mathbf{V}_a[v])\}$ between anchor-frame pixel coordinates \mathbf{u}_v and mesh vertices. Given camera intrinsics K , we estimate the camera pose (R, t) via robust PnP [71, 37, 4]:

$$(R^*, t^*) = \arg \min_{R, t} \sum_v \rho_v (\|\pi_K(R \mathbf{V}_a[v] + t) - \mathbf{u}_v\|_2) \quad (8)$$

Here π_K is the perspective projection and ρ_v is a robust weighting factor for each correspondence.

4D point tracking. Finally, we lift pixels to 3D by intersecting anchor-frame rays with the anchor mesh and tracking their barycentric coordinates over time. Because the animated mesh vertices $\{\hat{\mathbf{V}}^{(f)}\}_{f=1}^F$ from Section 4.2 reside in a canonical object space, we apply our estimated camera pose to align them with the input video. For a pixel \mathbf{u} with barycentric weights \mathbf{w} on face ϕ , its 3D trajectory in the anchor camera coordinates at frame f is calculated as:

$$\mathbf{X}_{\mathbf{u}}^{(f)} = R^* \sum_{i=0}^2 w_i \hat{\mathbf{V}}_{\mathcal{F}[\phi, i]}^{(f)} + t^* \quad (9)$$

This maps the canonical mesh deformation back into the observer’s frame of reference, yielding dense 3D trajectories for all foreground pixels across the video sequence.

5 Experiments

We evaluate our approach in three complementary settings that exercise the full attention chain introduced in Sec. 4: **(1) 4D mesh generation** (Sec. 5.1), **(2) 2D point tracking** on dynamic objects (Sec. 5.2), and **(3) world-coordinate 4D point tracking** (Sec. 5.3). We build on ActionMesh [59] as our base model (Sec.3) for all our experiments. For 2D and 4D tracking where videos have more than 16 frames, we used the autoregressive scaling method presented in Sec.4.3. All experiments ran on an H100 GPU.

5.1 4D Mesh Generation

Datasets and metrics. Following [59], we evaluate on *ActionBench* [59] and *Consistent4D* [26]. ActionBench contains 16-frame clips with ground-truth 4D meshes, while Consistent4D is used to evaluate out-of-distribution rendering quality. For geometry, we report end-to-end generation *Time*, *CD-3D* (per-frame), *CD-4D* (full 4D point cloud), *CD-M* (motion-only), and *Normal Consistency*. All predictions are aligned to ground truth with ICP before metric computation; results without ICP are provided in the supplement. For rendering, we report *LPIPS* [100], *CLIP* [55], and *DreamSim* [18] between rendered and ground-truth views.

Baselines. Following [59], we compare against state-of-the-art video-to-4D methods: Step1X-3D [39], L4GM [57], GVFD [96], LIM [58], DreamMesh4D (DM4D) [42], V2M4 [8], ShapeGen4D (SG4D) [90], and ActionMesh [59]. We also include image-to-3D models applied independently per frame: TripoSG [41] and TRELIS [82].

Quantitative results. Table 1(left) shows that our method achieves the best performance on three of four geometric ActionBench metrics: CD-3D (0.048), CD-4D (0.077), and Normal Consistency (0.97), while being over an order of magnitude faster: 9 s per 16-frame clip vs. 2 min for ActionMesh [59] ($\sim 14\times$) and 15 min for ShapeGen4D [90] ($\sim 100\times$). ActionMesh is slightly better on CD-M (0.148 vs. 0.163). On Consistent4D (Table 1 (right)), our method outperforms all non-aligned baselines, and with camera-pose estimation (*Ours + CPE*) it surpasses the aligned baseline L4GM [57]

Table 1: **Left:** ActionBench results. Our training-free approach is the fastest and achieves SoTA CD-3D, CD-4D, and Normal Consistency. **Right:** Consistent4D rendering results. With camera pose estimation (*Ours* + *CPE*), our method achieves the best LPIPS, CLIP, and DreamSim among 4D mesh generation methods.

ActionBench	Time (s)	CD-3D ↓	CD-4D ↓	CD-M ↓	Normal Consist. ↑	Consistent4D	Aligned	LPIPS ↓	CLIP ↑	Dream Sim ↓
TRELLIS [82]	900	0.065	0.181	–	–	Step1X-3D [39]	✗	0.1524	0.9040	0.1106
TripoSG [41]	120	0.056	0.184	–	–	L4GM [57]	✓	0.0988	0.9397	0.0487
DM4D [42]	2100	0.104	0.152	0.265	–	GVFD [96]	✗	0.1691	0.8601	0.1467
LIM [58]	900	0.089	0.126	0.243	–	SG4D [90]	✗	0.1359	0.9009	0.0966
V2M4 [8]	2100	0.068	0.340	0.616	–	ActionMesh [59]	✗	0.1458	0.9012	0.0939
SG4D [90]	900	0.060	0.170	0.348	0.91	Ours	✗	0.1423	0.9112	0.0823
ActionMesh [59]	120	0.053	0.081	0.148	0.85	Ours + CPE	✓	0.0823	0.9468	0.0319
Ours	9	0.048	0.077	0.163	0.97					

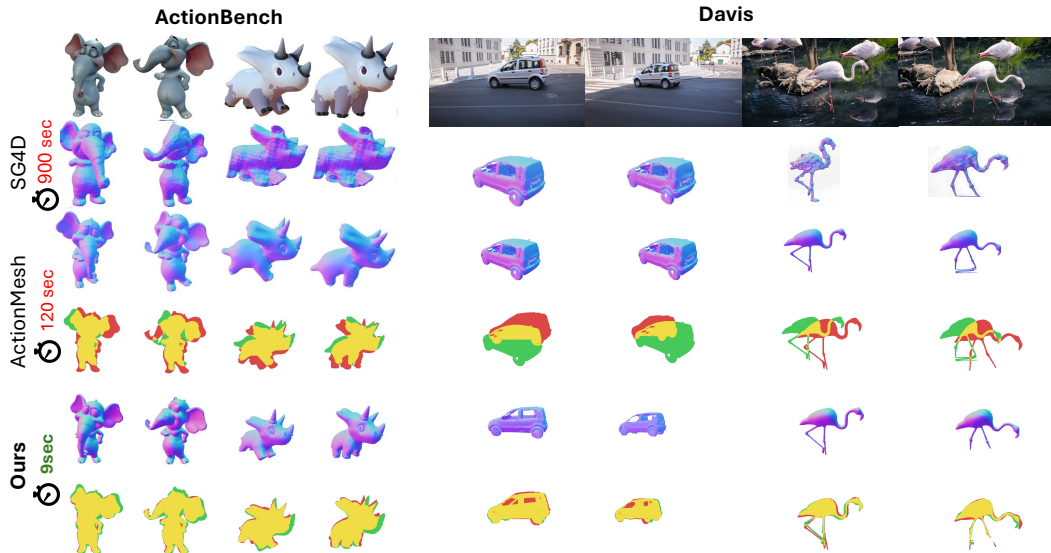


Figure 3: **4D Mesh Generation.** Our method produces sharp, temporally consistent meshes, aligns them to the input camera, and runs in **only 9 sec**, compared to 120–900 sec for prior methods. Unlike SG4D and ActionMesh, which generate object-centric meshes, our spatial attention-chain correspondences enable camera recovery and world placement, yielding high foreground overlap (yellow) and fewer mismatch regions (red/green).

on all metrics. These results demonstrate that our method produces high-quality, topology-consistent, and camera-aligned 4D meshes, without extra training or an additional network.

User study. We conducted 2,000 pairwise comparisons between our method and ActionMesh [59], with 100 raters judging appearance and motion consistency. Ours is preferred in 75% of comparisons. See Supp. for details.

Qualitative results. Fig. 3 shows that our method produces sharp, temporally consistent meshes while also uniquely aligning them to the input camera. Unlike ActionMesh and ShapeGen4D, which generate object-centric meshes with clear silhouette mismatch, our attention-chain correspondences provide dense 2D ↔ 3D matches for PnP camera recovery. This yields accurate image alignment (yellow regions) and directly enables 4D tracking and camera-aware applications.

5.2 2D Point Tracking

Datasets and metrics. Our pipeline follows ActionMesh [59] in reconstructing a single dynamic object rather than the full scene, so we evaluate 2D tracking on foreground object points only. We use *BADJA* [3], a standard articulated-animal joint-tracking benchmark, and a foreground-only version

Table 2: **Point tracking results.** (a) and (b): 2D point tracking on DAVIS-foreground and BADJA. (c): 4D point tracking on PointOdyssey (PO) and Dynamic Replica (DR).

(a) 2D Tracking (DAVIS)				(b) 2D Tracking (BADJA)			(c) 4D Tracking		
	AJ	$\langle\delta\rangle_{\text{avg}}$	OA		segA	$\delta^{3\text{px}}$		PO	DR
<i>Supervised</i>				<i>Supervised</i>			<i>Supervised</i>		
BootsTAP [13]	56.64	69.99	87.88	TAP-Net [12]	54.4	6.3	St4RTrack [17]	72.04	76.82
SpatialTracker [84]	54.97	71.51	85.64	PIPs [20]	61.9	13.5	TraceAny. [47]	47.02	61.19
CowTracker [35]	60.08	73.53	88.64	TAPIR [14]	66.9	15.2	Any4D [32]	64.25	70.33
<i>Zero-shot</i>				<i>Zero-shot</i>			<i>Zero-shot</i>		
DiffTrack [51]	26.44	43.01	72.10	OmniMotion [75]	57.2	13.2	4RC [49]	66.92	76.11
DenoiseToTrack [92]	35.15	50.12	75.16	CoTracker [31]	63.6	18.0	V-DPM [66]	82.12	78.18
Ours	53.33	66.34	90.41	SpatialTracker [84]	69.2	17.1			
				<i>Zero-shot</i>			<i>Zero-shot</i>		
				Ours			Ours		
							ActionMesh (II) [59]		
							31.5 41.6		
							59.9 65.3		

of *TAP-Vid-DAVIS* [12, 54]. Following [12], we report Average Jaccard (*AJ*), average position accuracy ($\langle\delta\rangle_{\text{avg}}$), and Occlusion Accuracy (*OA*). On BADJA, we report segmentation accuracy on joint trajectories (*segA*) and the fraction of predictions within 3 px of ground truth ($\delta^{3\text{px}}$).

Baselines. We compare with three groups of trackers: *2D-supervised* methods, including BootsTAP [13], TAPIR [14], CoTracker [31], TAP-Net [12], PIPs [20], OmniMotion [75], and CowTracker [35]; *3D-aware* trackers that lift 2D tracks into 3D, including SpatialTracker [84]; and *zero-shot* feature-based trackers from pretrained diffusion models, DiffTrack [51] and Denoise-to-Track [92].

Results. Table 2(a) shows that our method is the strongest zero-shot tracker on DAVIS-foreground, outperforming DiffTrack and Denoise-to-Track on all metrics. It also achieves the best OA overall (90.41), while remaining competitive with supervised trackers. Table 2(b), on the BADJA benchmark, our zero-shot method remains close to supervised trackers, outperforming several of them despite using no tracking supervision. These results show that attention-chain correspondences provide strong 2D tracking directly from the frozen 4D generation backbone.

5.3 4D Point Tracking

Datasets and metrics. We follow the dynamic-only protocol of the WorldTrack benchmark [17] and evaluate on *PointOdyssey (PO)* [101] and *Dynamic Replica (DR)* [30]. We report APD_{3D} , the percentage of predictions within a set of 3D distance thresholds, averaged over thresholds after global median alignment.

Baselines. We compare against ActionMesh Stage II [59] as a zero-shot baseline for per-frame mesh tracking, and five supervised 4D trackers: V-DPM [66], 4RC [49], Any4D [32], TraceAnything [47], and St4RTrack [17].

Results. Tab. 2(c) shows that our method substantially improves over the zero-shot ActionMesh Stage II baseline on both datasets (+28.4 APD_{3D} on PO and +23.7 on DR). This demonstrates that attention-chain correspondences, together with camera estimation, provide a much stronger signal for world-coordinate 4D tracking. Despite using no 4D tracking supervision, our method is competitive with supervised trackers: it outperforms TraceAnything and approaches Any4D and 4RC. Our approach close a large part of the gap without task-specific training.

6 Conclusion

In this paper, we introduced a training-free framework for fast video-to-4D-mesh reconstruction. By exposing spatio-temporal attention chains inside a frozen 4D backbone, we recover correspondences that animate an anchor mesh without a learned deformation network. The same mechanism yields *topology-consistent meshes*, *faster inference*, *longer rollouts*, and enables *2D/4D tracking with camera recovery*. At the same time, our framework inherits the limitations of the frozen models it builds on. Mesh quality depends on the image-to-3D model and denoiser; sparse smoothing and local-rigid deformation can damp fine motion; and multi-minute rollouts may still degrade as errors accumulate and attention over generated anchors becomes increasingly diffuse.

References

- [1] S. Abnar and W. Zuidema. Quantifying attention flow in transformers. In *Proceedings of the 58th Annual Meeting of the Association for Computational Linguistics*, pages 4190–4197. Association for Computational Linguistics, July 2020.
- [2] Y. Atzmon, R. Gal, Y. Tewel, Y. Kasten, and G. Chechik. Identity-motion trade-offs in text-to-video generation. In *36th British Machine Vision Conference 2025, BMVC, 2025*.
- [3] B. Biggs, T. Roddick, A. Fitzgibbon, and R. Cipolla. Creatures great and SMAL: Recovering the shape and motion of animals from video. In *ACCV*, 2018.
- [4] R. C. Bolles and M. A. Fischler. A ransac-based approach to model fitting and its application to finding cylinders in range data. In *Ijcai*, volume 1981, pages 637–643, 1981.
- [5] M. Cao, X. Wang, Z. Qi, Y. Shan, X. Qie, and Y. Zheng. Masactrl: Tuning-free mutual self-attention control for consistent image synthesis and editing. In *Proceedings of the IEEE/CVF international conference on computer vision*, pages 22560–22570, 2023.
- [6] W. Cao, C. Luo, B. Zhang, M. Nießner, and J. Tang. Motion2vecsets: 4d latent vector set diffusion for non-rigid shape reconstruction and tracking. In *Proceedings of the IEEE/CVF conference on computer vision and pattern recognition*, pages 20496–20506, 2024.
- [7] H. Chefer, S. Gur, and L. Wolf. Generic attention-model explainability for interpreting bi-modal and encoder-decoder transformers. In *Proceedings of the IEEE/CVF International Conference on Computer Vision (ICCV)*, pages 397–406, October 2021.
- [8] J. Chen, B. Zhang, X. Tang, and P. Wonka. V2m4: 4d mesh animation reconstruction from a single monocular video. In *Proceedings of the IEEE/CVF International Conference on Computer Vision*, pages 11643–11653, 2025.
- [9] R. Chen, J. Zhang, Y. Liang, G. Luo, W. Li, J. Liu, X. Li, X. Long, J. Feng, and P. Tan. Dora: Sampling and benchmarking for 3d shape variational auto-encoders. In *Proceedings of the Computer Vision and Pattern Recognition Conference (CVPR)*, pages 16251–16261, June 2025.
- [10] X. Chen, Y. Chen, Y. Xiu, A. Geiger, and A. Chen. Easi3r: Estimating disentangled motion from dust3r without training. In *Proceedings of the IEEE/CVF International Conference on Computer Vision*, pages 9158–9168, 2025.
- [11] S. Cho, J. Huang, J. Nam, H. An, S. Kim, and J.-Y. Lee. Local all-pair correspondence for point tracking. In *European conference on computer vision*, pages 306–325. Springer, 2024.
- [12] C. Doersch, A. Gupta, L. Markeeva, A. Recasens, L. Smaira, Y. Aytar, J. Carreira, A. Zisserman, and Y. Yang. Tap-vid: A benchmark for tracking any point in a video. *Advances in Neural Information Processing Systems*, 35:13610–13626, 2022.
- [13] C. Doersch, P. Luc, Y. Yang, D. Gokay, S. Koppula, A. Gupta, J. Heyward, I. Rocco, R. Goroshin, J. Carreira, et al. Bootstap: Bootstrapped training for tracking-any-point. In *Proceedings of the Asian Conference on Computer Vision*, pages 3257–3274, 2024.
- [14] C. Doersch, Y. Yang, M. Vecerik, D. Gokay, A. Gupta, Y. Aytar, J. Carreira, and A. Zisserman. Tapir: Tracking any point with per-frame initialization and temporal refinement. In *Proceedings of the IEEE/CVF International Conference on Computer Vision*, pages 10061–10072, 2023.
- [15] N. S. Dutt, S. Muralikrishnan, and N. J. Mitra. Diffusion 3d features (diff3f): Decorating untextured shapes with distilled semantic features. In *Proceedings of the IEEE/CVF Conference on Computer Vision and Pattern Recognition (CVPR)*, pages 4494–4504, June 2024.
- [16] Y. Erel, O. Dünkler, R. Dabral, V. Golyanik, C. Theobalt, and A. H. Bermano. Attention (as discrete-time markov) chains. In *The Thirty-ninth Annual Conference on Neural Information Processing Systems*, 2026.
- [17] H. Feng, J. Zhang, Q. Wang, Y. Ye, P. Yu, M. J. Black, T. Darrell, and A. Kanazawa. St4rtrack: Simultaneous 4d reconstruction and tracking in the world. In *Proceedings of the IEEE/CVF International Conference on Computer Vision*, pages 8503–8513, 2025.
- [18] S. Fu, N. Tamir, S. Sundaram, L. Chai, R. Zhang, T. Dekel, and P. Isola. Dreamsim: Learning new dimensions of human visual similarity using synthetic data. In *Advances in Neural Information Processing Systems*, volume 36, pages 50742–50768, 2023.

- [19] Z. Guo, J. Xiang, K. Ma, W. Zhou, H. Li, and R. Zhang. Make-it-animatable: An efficient framework for authoring animation-ready 3d characters. In *Proceedings of the Computer Vision and Pattern Recognition Conference*, pages 10783–10792, 2025.
- [20] A. W. Harley, Z. Fang, and K. Fragkiadaki. Particle video revisited: Tracking through occlusions using point trajectories. In *European Conference on Computer Vision*, pages 59–75. Springer, 2022.
- [21] A. W. Harley, Y. You, X. Sun, Y. Zheng, N. Raghuraman, Y. Gu, S. Liang, W.-H. Chu, A. Dave, S. You, et al. Alltracker: Efficient dense point tracking at high resolution. In *Proceedings of the IEEE/CVF International Conference on Computer Vision*, pages 5253–5262, 2025.
- [22] A. Hertz, R. Mokady, J. Tenenbaum, K. Aberman, Y. Pritch, and D. Cohen-Or. Prompt-to-prompt image editing with cross attention control. *arXiv preprint arXiv:2208.01626*, 2022.
- [23] Y. Hong, K. Zhang, J. Gu, S. Bi, Y. Zhou, D. Liu, F. Liu, K. Sunkavalli, T. Bui, and H. Tan. Lrm: Large reconstruction model for single image to 3d. *arXiv preprint arXiv:2311.04400*, 2023.
- [24] H. Jeong, C.-H. P. Huang, J. C. Ye, N. J. Mitra, and D. Ceylan. Track4gen: Teaching video diffusion models to track points improves video generation. In *Proceedings of the IEEE/CVF Conference on Computer Vision and Pattern Recognition (CVPR)*, 2025.
- [25] Y. Jiang, C. Yu, C. Cao, F. Wang, W. Hu, and J. Gao. Animate3d: Animating any 3d model with multi-view video diffusion. *Advances in Neural Information Processing Systems*, 37:125879–125906, 2024.
- [26] Y. Jiang, L. Zhang, J. Gao, W. Hu, and Y. Yao. Consistent4d: Consistent 360° dynamic object generation from monocular video. In *The Twelfth International Conference on Learning Representations*, 2024.
- [27] Z. Jiang, C. Zheng, I. Laina, D. Larlus, and A. Vedaldi. Mesh4d: 4d mesh reconstruction and tracking from monocular video. *arXiv preprint arXiv:2601.05251*, 2026.
- [28] L. Jin, R. Tucker, Z. Li, D. Fouhey, N. Snavely, and A. Holynski. Stereo4d: Learning how things move in 3d from internet stereo videos. In *Proceedings of the Computer Vision and Pattern Recognition Conference*, pages 10497–10509, 2025.
- [29] N. Karaev, Y. Makarov, J. Wang, N. Neverova, A. Vedaldi, and C. Rupprecht. Cotracker3: Simpler and better point tracking by pseudo-labelling real videos. In *Proceedings of the IEEE/CVF International Conference on Computer Vision*, pages 6013–6022, 2025.
- [30] N. Karaev, I. Rocco, B. Graham, N. Neverova, A. Vedaldi, and C. Rupprecht. Dynamicstereo: Consistent dynamic depth from stereo videos. *CVPR*, 2023.
- [31] N. Karaev, I. Rocco, B. Graham, N. Neverova, A. Vedaldi, and C. Rupprecht. Cotracker: It is better to track together. In *European conference on computer vision*, pages 18–35. Springer, 2024.
- [32] J. Karhade, N. Keetha, Y. Zhang, T. Gupta, A. Sharma, S. Scherer, and D. Ramanan. Any4d: Unified feed-forward metric 4d reconstruction. *arXiv preprint arXiv:2512.10935*, 2025.
- [33] Y. Kasten, W. Lu, and H. Maron. Fast encoder-based 3d from casual videos via point track processing. *Advances in Neural Information Processing Systems*, 37:96150–96180, 2024.
- [34] M. Kwon, J. Choi, J. Park, S. Jeon, J. Jang, J. Seo, M.-S. Kwak, J.-H. Kim, and S. Kim. Cameo: Correspondence-attention alignment for multi-view diffusion models. In *Proceedings of the IEEE/CVF Conference on Computer Vision and Pattern Recognition (CVPR)*, 2026.
- [35] Z. Lai, E. Insafutdinov, E. Sucar, and A. Vedaldi. Cowtracker: Tracking by warping instead of correlation. *arXiv preprint arXiv:2602.04877*, 2026.
- [36] G. Le Moing, J. Ponce, and C. Schmid. Dense optical tracking: Connecting the dots. In *Proceedings of the IEEE/CVF Conference on Computer Vision and Pattern Recognition*, pages 19187–19197, 2024.
- [37] V. Lepetit, F. Moreno-Noguer, and P. Fua. Epanp: Efficient perspective-n-point camera pose estimation. *Int. J. Comput. Vis.*, 81(2):155–166, 2009.
- [38] W. Li, J. Liu, H. Yan, R. Chen, Y. Liang, X. Chen, P. Tan, and X. Long. Craftsman3d: High-fidelity mesh generation with 3d native diffusion and interactive geometry refiner. In *Proceedings of the Computer Vision and Pattern Recognition Conference*, pages 5307–5317, 2025.

- [39] W. Li, X. Zhang, Z. Sun, D. Qi, H. Li, W. Cheng, W. Cai, S. Wu, J. Liu, Z. Wang, et al. Step1x-3d: Towards high-fidelity and controllable generation of textured 3d assets. *arXiv preprint arXiv:2505.07747*, 2025.
- [40] X. Li, F. Zhang, J. Pan, Y. Hou, V. Y. F. Tan, and Z. Yang. Enhancing long video generation consistency without tuning. *arXiv preprint arXiv:2412.17254*, 2024. ICML 2025 Workshop on Building Physically Plausible World Models.
- [41] Y. Li, Z.-X. Zou, Z. Liu, D. Wang, Y. Liang, Z. Yu, X. Liu, Y.-C. Guo, D. Liang, W. Ouyang, et al. Triposg: High-fidelity 3d shape synthesis using large-scale rectified flow models. *arXiv preprint arXiv:2502.06608*, 2025.
- [42] Z. Li, Y. Chen, and P. Liu. Dreammesh4d: Video-to-4d generation with sparse-controlled gaussian-mesh hybrid representation. *Advances in Neural Information Processing Systems*, 37:21377–21400, 2024.
- [43] Z. Li, R. Tucker, F. Cole, Q. Wang, L. Jin, V. Ye, A. Kanazawa, A. Holynski, and N. Snavely. Megasam: Accurate, fast and robust structure and motion from casual dynamic videos. In *Proceedings of the IEEE/CVF Conference on Computer Vision and Pattern Recognition*, pages 10486–10496, 2025.
- [44] H. Liang, Y. Yin, D. Xu, H. Liang, Z. Wang, K. N. Plataniotis, Y. Zhao, and Y. Wei. Diffusion4d: Fast spatial-temporal consistent 4d generation via video diffusion models. *arXiv preprint arXiv:2405.16645*, 2024.
- [45] H. Lin, S. Chen, J. H. Liew, D. Y. Chen, Z. Li, G. Shi, J. Feng, and B. Kang. Depth anything 3: Recovering the visual space from any views. *arXiv preprint arXiv:2511.10647*, 2025.
- [46] I. Liu, Z. Xu, Y. Wang, H. Tan, Z. Xu, X. Wang, H. Su, and Z. Shi. Riganything: Template-free autoregressive rigging for diverse 3d assets. *ACM Transactions on Graphics (TOG)*, 44(4):1–12, 2025.
- [47] X. Liu, Y. Xiao, D. Y. Chen, J. Feng, Y.-W. Tai, C.-K. Tang, and B. Kang. Trace anything: Representing any video in 4d via trajectory fields. *arXiv preprint arXiv:2510.13802*, 2025.
- [48] R. Lu, Y. Chen, Y. Liu, J. Tang, J. Ni, D. Wan, G. Zeng, and S. Huang. Taco: Taming diffusion for in-the-wild video amodal completion. *Proceedings of the IEEE/CVF International Conference on Computer Vision*, 2025.
- [49] Y. Luo, S. Zhou, Y. Lan, X. Pan, and C. C. Loy. Arc: 4d reconstruction via conditional querying anytime and anywhere. *arXiv preprint arXiv:2602.10094*, 2026.
- [50] S. Muralikrishnan, N. S. Dutt, and N. J. Mitra. Smf: Template-free and rig-free animation transfer using kinetic codes. *ACM Transactions on Graphics (TOG)*, 44(6), 2025.
- [51] J. Nam, S. Son, D. Chung, J. Kim, S. Jin, J. Hur, and S. Kim. Emergent temporal correspondences from video diffusion transformers. In *Advances in Neural Information Processing Systems (NeurIPS)*, 2025.
- [52] M. Oquab, T. Darcet, T. Moutakanni, H. V. Vo, M. Szafraniec, V. Khalidov, P. Fernandez, D. Haziza, F. Massa, A. El-Nouby, M. Assran, N. Ballas, W. Galuba, R. Howes, P.-Y. B. Huang, S.-W. Li, I. Misra, M. G. Rabbat, V. Sharma, G. Synnaeve, H. Xu, H. Jégou, J. Mairal, P. Labatut, A. Joulin, and P. Bojanowski. Dinov2: Learning robust visual features without supervision. *TMLR*, 2024.
- [53] A. Pondaven, A. Siarohin, S. Tulyakov, P. Torr, and F. Pizzati. Video motion transfer with diffusion transformers. In *Proceedings of the IEEE/CVF Conference on Computer Vision and Pattern Recognition (CVPR)*, 2025.
- [54] J. Pont-Tuset, F. Perazzi, S. Caelles, P. Arbeláez, A. Sorkine-Hornung, and L. Van Gool. The 2017 davis challenge on video object segmentation. *arXiv preprint arXiv:1704.00675*, 2017.
- [55] A. Radford, J. W. Kim, C. Hallacy, A. Ramesh, G. Goh, S. Agarwal, G. Sastry, A. Askell, P. Mishkin, J. Clark, G. Krueger, and I. Sutskever. Learning transferable visual models from natural language supervision. In *ICML*, 2021.
- [56] J. Ren, L. Pan, J. Tang, C. Zhang, A. Cao, G. Zeng, and Z. Liu. Dreamgaussian4d: Generative 4d gaussian splatting. *arXiv preprint arXiv:2312.17142*, 2023.
- [57] J. Ren, K. Xie, A. Mirzaei, H. Liang, X. Zeng, K. Kreis, Z. Liu, A. Torralba, S. Fidler, S. W. Kim, et al. L4gm: Large 4d gaussian reconstruction model. *Advances in Neural Information Processing Systems*, 37:56828–56858, 2024.

- [58] R. Sabathier, N. J. Mitra, and D. Novotny. Lim: Large interpolator model for dynamic reconstruction. In *Proceedings of the Computer Vision and Pattern Recognition Conference*, pages 6154–6164, 2025.
- [59] R. Sabathier, D. Novotny, N. J. Mitra, and T. Monnier. Actionmesh: Animated 3d mesh generation with temporal 3d diffusion. *arXiv preprint arXiv:2601.16148*, 2026.
- [60] D. Samuel, M. Levy, N. Darshan, G. Chechik, and R. Ben-Ari. Omnimatezero: Fast training-free omnimate with pre-trained video diffusion models. In *SIGGRAPH Asia 2025 Conference Papers*, 2025.
- [61] Y. Shi, Y. Liu, Y. Wu, X. Liu, C. Zhao, J. Luo, and B. Zhou. Drive any mesh: 4d latent diffusion for mesh deformation from video. *arXiv preprint arXiv:2506.07489*, 2025.
- [62] A. Shrivastava, S. Mehta, D. Geng, and A. Owens. Point prompting: Counterfactual tracking with video diffusion models. In *International Conference on Learning Representations*, 2026.
- [63] Y. Siddiqui, T. Monnier, F. Kokkinos, M. Kariya, Y. Kleiman, E. Garreau, O. Gafni, N. Neverova, A. Vedaldi, R. Shapovalov, et al. Meta 3d assetgen: Text-to-mesh generation with high-quality geometry, texture, and pbr materials. *Advances in Neural Information Processing Systems*, 37:9532–9564, 2024.
- [64] C. Song, J. Zhang, X. Li, F. Yang, Y. Chen, Z. Xu, J. H. Liew, X. Guo, F. Liu, J. Feng, et al. Magicarticulate: Make your 3d models articulation-ready. In *Proceedings of the Computer Vision and Pattern Recognition Conference*, pages 15998–16007, 2025.
- [65] O. Sorkine and M. Alexa. As-rigid-as-possible surface modeling. In *Proceedings of the Fifth Eurographics Symposium on Geometry Processing*, 2007.
- [66] E. Sucar, E. Insafutdinov, Z. Lai, and A. Vedaldi. V-DPM: 4d video reconstruction with dynamic point maps. In *Proceedings of the IEEE/CVF Conference on Computer Vision and Pattern Recognition (CVPR)*, 2026.
- [67] R. W. Sumner, J. Schmid, and M. Pauly. Embedded deformation for shape manipulation. In *ACM siggraph 2007 papers*. 2007.
- [68] J. Tang, Z. Chen, X. Chen, T. Wang, G. Zeng, and Z. Liu. Lgm: Large multi-view gaussian model for high-resolution 3d content creation. In *European Conference on Computer Vision*, pages 1–18. Springer, 2024.
- [69] L. Tang, M. Jia, Q. Wang, C. P. Phoo, and B. Hariharan. Emergent correspondence from image diffusion. *Advances in neural information processing systems*, 36:1363–1389, 2023.
- [70] T. H. Team. Hunyuan3d 2.5: Towards high-fidelity 3d assets generation with ultimate details, 2025.
- [71] G. Terzakis and M. Lourakis. A consistently fast and globally optimal solution to the perspective-n-point problem. In *European Conference on Computer Vision*, pages 478–494. Springer, 2020.
- [72] Y. Tewel, O. Kaduri, R. Gal, Y. Kasten, L. Wolf, G. Chechik, and Y. Atzmon. Training-free consistent text-to-image generation. *ACM Transactions on Graphics (TOG)*, 43(4):1–18, 2024.
- [73] N. Tumanyan, M. Geyer, S. Bagon, and T. Dekel. Plug-and-play diffusion features for text-driven image-to-image translation. In *Proceedings of the IEEE/CVF Conference on Computer Vision and Pattern Recognition (CVPR)*, pages 1921–1930, June 2023.
- [74] J. Wang, M. Chen, N. Karaev, A. Vedaldi, C. Rupprecht, and D. Novotny. Vggt: Visual geometry grounded transformer. In *Proceedings of the Computer Vision and Pattern Recognition Conference*, pages 5294–5306, 2025.
- [75] Q. Wang, Y.-Y. Chang, R. Cai, Z. Li, B. Hariharan, A. Holynski, and N. Snavely. Tracking everything everywhere all at once. In *Proceedings of the IEEE/CVF International Conference on Computer Vision*, pages 19795–19806, 2023.
- [76] Q. Wang, Y. Zhang, A. Holynski, A. A. Efros, and A. Kanazawa. Continuous 3d perception model with persistent state. In *Proceedings of the Computer Vision and Pattern Recognition Conference*, pages 10510–10522, 2025.
- [77] S. Wang, V. Leroy, Y. Cabon, B. Chidlovskii, and J. Revaud. Dust3r: Geometric 3d vision made easy. In *Proceedings of the IEEE/CVF conference on computer vision and pattern recognition*, pages 20697–20709, 2024.

- [78] Y. Wang, X. Wang, Z. Chen, Z. Wang, F. Sun, and J. Zhu. Vidu4d: Single generated video to high-fidelity 4d reconstruction with dynamic gaussian surfels. *Advances in Neural Information Processing Systems*, 37:131316–131343, 2024.
- [79] R. Wu, R. Gao, B. Poole, A. Trevithick, C. Zheng, J. T. Barron, and A. Holynski. Cat4d: Create anything in 4d with multi-view video diffusion models. In *Proceedings of the IEEE/CVF Conference on Computer Vision and Pattern Recognition*, pages 26057–26068, 2025.
- [80] Z. Wu, C. Yu, Y. Jiang, C. Cao, F. Wang, and X. Bai. Sc4d: Sparse-controlled video-to-4d generation and motion transfer. In *European Conference on Computer Vision*, pages 361–379. Springer, 2024.
- [81] Z. Wu, C. Yu, F. Wang, and X. Bai. Animateanymesh: A feed-forward 4d foundation model for text-driven universal mesh animation. In *Proceedings of the IEEE/CVF International Conference on Computer Vision*, pages 13557–13568, 2025.
- [82] J. Xiang, Z. Lv, S. Xu, Y. Deng, R. Wang, B. Zhang, D. Chen, X. Tong, and J. Yang. Structured 3d latents for scalable and versatile 3d generation. In *Proceedings of the IEEE/CVF conference on computer vision and pattern recognition*, pages 21469–21480, 2025.
- [83] Y. Xiao, J. Wang, N. Xue, N. Karaev, Y. Makarov, B. Kang, X. Zhu, H. Bao, Y. Shen, and X. Zhou. Spatialtrackerv2: 3d point tracking made easy. *arXiv preprint arXiv:2507.12462*, 2025.
- [84] Y. Xiao, Q. Wang, S. Zhang, N. Xue, S. Peng, Y. Shen, and X. Zhou. Spatialtracker: Tracking any 2d pixels in 3d space. In *Proceedings of the IEEE/CVF Conference on Computer Vision and Pattern Recognition*, pages 20406–20417, 2024.
- [85] Y. Xie, C.-H. Yao, V. Voleti, H. Jiang, and V. Jampani. SV4D: Dynamic 3d content generation with multi-frame and multi-view consistency. *arXiv preprint arXiv:2407.17470*, 2024.
- [86] T.-X. Xu, X. Gao, W. Hu, X. Li, S.-H. Zhang, and Y. Shan. Geometrycrafter: Consistent geometry estimation for open-world videos with diffusion priors. In *Proceedings of the IEEE/CVF International Conference on Computer Vision*, pages 6632–6644, 2025.
- [87] Z. Xu, Z. Li, Z. Dong, X. Zhou, R. Newcombe, and Z. Lv. 4dgt: Learning a 4d gaussian transformer using real-world monocular videos. 2025.
- [88] C.-H. Yao, Y. Xie, V. Voleti, H. Jiang, and V. Jampani. Sv4d 2.0: Enhancing spatio-temporal consistency in multi-view video diffusion for high-quality 4d generation. In *Proceedings of the IEEE/CVF International Conference on Computer Vision*, pages 13248–13258, 2025.
- [89] Y. Yao, Z. Deng, and J. Hou. Riggs: Rigging of 3d gaussians for modeling articulated objects in videos. In *CVPR*, 2025.
- [90] J. Yenphraphai, A. Mirzaei, J. Chen, J. Zou, S. Tulyakov, R. A. Yeh, P. Wonka, and C. Wang. Shapegen4d: Towards high quality 4d shape generation from videos. *arXiv preprint arXiv:2510.06208*, 2025.
- [91] Y. Yin, D. Xu, Z. Wang, Y. Zhao, and Y. Wei. 4dgen: Grounded 4d content generation with spatial-temporal consistency. *arXiv preprint arXiv:2312.17225*, 2023.
- [92] T. Yuan, Y. Yang, L.-Z. Chen, Y. Yao, and Z. Qian. Denoise to track: Harnessing video diffusion priors for robust correspondence. *arXiv preprint arXiv:2512.04619*, 2025.
- [93] Y. Zeng, Y. Jiang, S. Zhu, Y. Lu, Y. Lin, H. Zhu, W. Hu, X. Cao, and Y. Yao. Stag4d: Spatial-temporal anchored generative 4d gaussians. In *European Conference on Computer Vision*, pages 163–179. Springer, 2024.
- [94] B. Zhang, L. Ke, A. W. Harley, and K. Fragkiadaki. Tapip3d: Tracking any point in persistent 3d geometry. *arXiv preprint arXiv:2504.14717*, 2025.
- [95] B. Zhang, J. Tang, M. Niessner, and P. Wonka. 3dshape2vecset: A 3d shape representation for neural fields and generative diffusion models. *ACM Transactions On Graphics (TOG)*, 42(4):1–16, 2023.
- [96] B. Zhang, S. Xu, C. Wang, J. Yang, F. Zhao, D. Chen, and B. Guo. Gaussian variation field diffusion for high-fidelity video-to-4d synthesis. *arXiv preprint arXiv:2507.23785*, 2025.
- [97] H. Zhang, X. Chen, Y. Wang, X. Liu, Y. Wang, and Y. Qiao. 4diffusion: Multi-view video diffusion model for 4d generation. *Advances in Neural Information Processing Systems*, 37:15272–15295, 2024.

- [98] J. Zhang, C. Herrmann, J. Hur, V. Jampani, T. Darrell, F. Cole, D. Sun, and M.-H. Yang. Monst3r: A simple approach for estimating geometry in the presence of motion. *arXiv preprint arXiv:2410.03825*, 2024.
- [99] L. Zhang, Z. Wang, Q. Zhang, Q. Qiu, A. Pang, H. Jiang, W. Yang, L. Xu, and J. Yu. Clay: A controllable large-scale generative model for creating high-quality 3d assets. *ACM Transactions on Graphics (TOG)*, 43(4):1–20, 2024.
- [100] R. Zhang, P. Isola, A. A. Efros, E. Shechtman, and O. Wang. The unreasonable effectiveness of deep features as a perceptual metric. In *Proceedings of the IEEE conference on computer vision and pattern recognition*, pages 586–595, 2018.
- [101] Y. Zheng, A. W. Harley, B. Shen, G. Wetzstein, and L. J. Guibas. Pointodyssey: A large-scale synthetic dataset for long-term point tracking. In *Proceedings of the IEEE/CVF International Conference on Computer Vision*, pages 19855–19865, 2023.

Supplementary Material

A Additional Qualitative Results

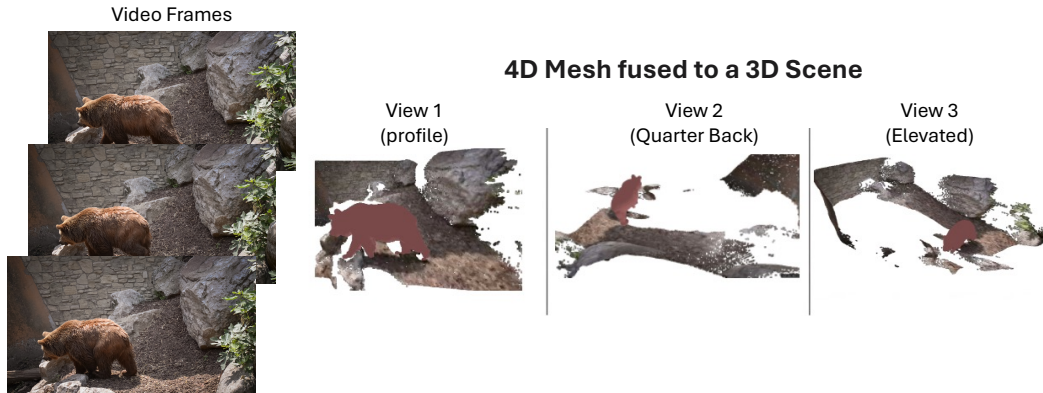


Figure 4: **Video-to-4D Scene Alignment.** Given our generated 4D object and a reconstructed background scene, we align the object to the environment using our dense 2D-to-3D correspondences. While this example utilizes Depth Anything V3 [45], our alignment framework is completely agnostic and functions seamlessly with any underlying scene reconstruction method. Please refer to our supplementary website for interactive, dynamic visualizations.

We provide additional qualitative comparisons that complement the quantitative evaluation in the main paper. These results further demonstrate the advantages of our training-free attention-chain framework across four settings: 4D mesh generation, long-sequence rollout, 2D point tracking, and 4D mesh placement in reconstructed scenes.

4D mesh generation. Figure 5 presents additional side-by-side comparisons between ActionMesh [59] and our method on sequences from ActionBench and in-the-wild videos. Our approach consistently produces comparable to better geometry with fewer temporal artifacts, while running in only 9 s per clip compared to ActionMesh’s 120 s. Unlike ActionMesh, which generate object-centric meshes, our spatial attention-chain correspondences enable camera recovery and world placement, yielding high foreground overlap (yellow) and fewer mismatch regions (red/green)

Long-sequence generation. Figure 6 shows autoregressive rollouts spanning 240 frames. ActionMesh accumulates drift over successive windows, leading to progressive geometry degradation and loss of recognizable structure. In contrast, our correspondence reinforcement (Sec. 4.3) maintains stable mesh quality throughout the sequence, preserving both global pose and fine detail even at frame 240.

2D point tracking. Figure 7 compares our zero-shot 2D point tracking against Denoise-to-Track [92], the current zero-shot state of the art. Each colored dot represents a tracked query point, with trails showing the predicted trajectory. Our method produces smoother, more accurate trajectories that better follow the underlying surface motion, particularly on articulated body parts where attention-chain correspondences provide geometrically grounded matches rather than purely appearance-based ones.

4D mesh placement. Figure 4 demonstrates that our camera pose estimation enables fusing the generated 4D mesh directly into a reconstructed 3D scene. Given only the input video frames, we recover the camera trajectory via PnP and place the animated mesh into a scene point cloud, allowing it to be viewed from arbitrary novel viewpoints. The mesh correctly occupies the physical space of the subject across all views, confirming that our attention-chain correspondences provide accurate world-space localization without any pose supervision. An interactive version with full camera control is available on the supplementary website.

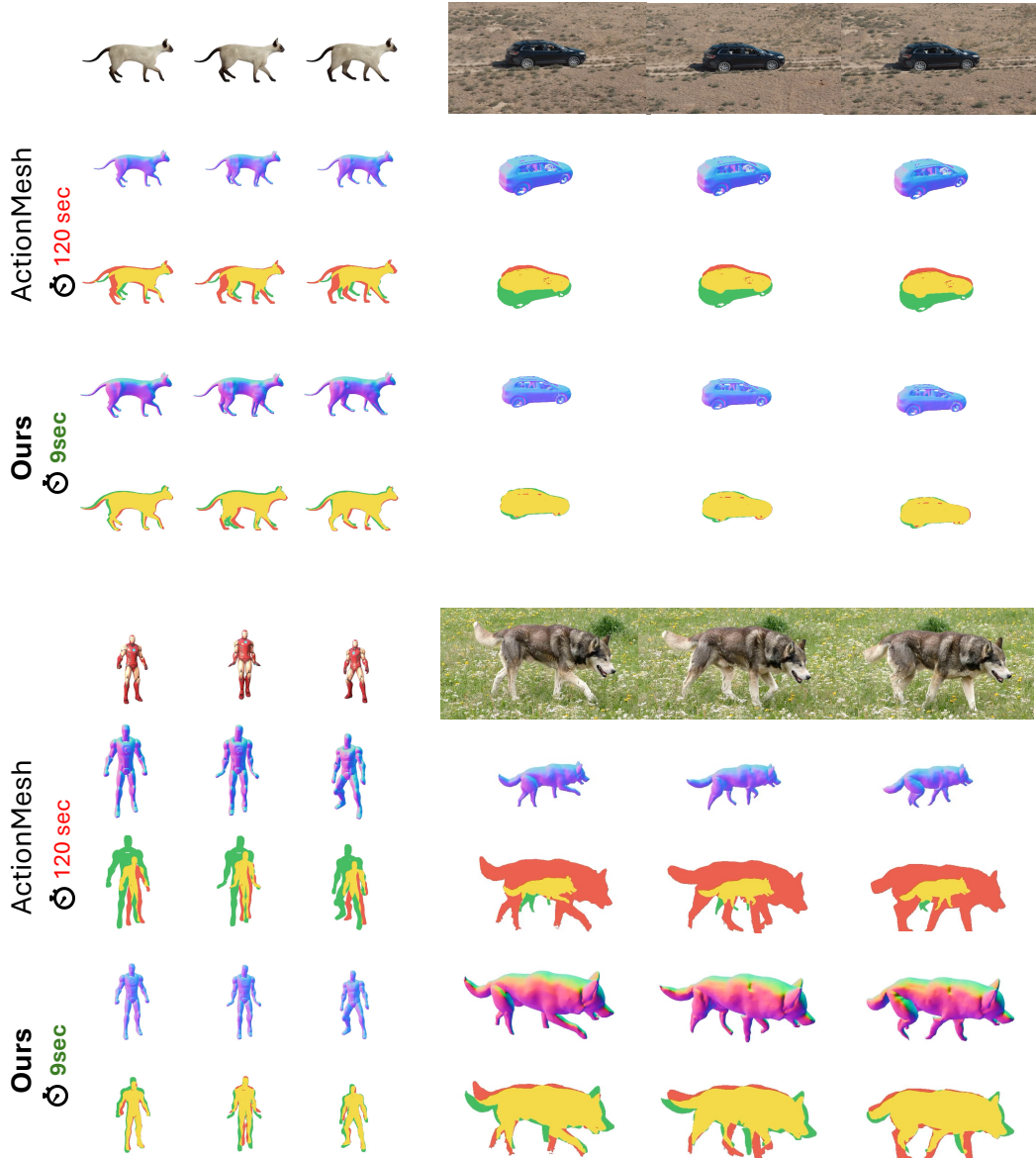


Figure 5: **Additional 4D mesh generation results.** Side-by-side comparison of ActionMesh [59] (left of each pair) and our method (right) on diverse ActionBench sequences. Each row shows a different input video. Our method produces sharper, temporally consistent meshes with fewer distortions while requiring only 9 s per clip vs. 120 s for ActionMesh.

B Ablation Study

We probe three design choices: (i) the number of Stage I denoising steps, (ii) the resulting per-clip wall-clock vs. ActionMesh, and (iii) the contribution of each component on long, 240-frame sequences. Unless stated otherwise we evaluate on ActionBench with the same protocol as Section 5.1.

Denoising steps vs. quality. Both methods share the same Stage I temporal denoiser Φ_θ ; ActionMesh further runs a learned Stage II that regularises the per-frame latents Z , while ours reads the attention of the *last* denoising step and propagates it through the chain $\mathbf{V} \rightarrow \mathbf{T} \rightarrow \mathbf{T} \rightarrow \mathbf{V}$. Figure 8 plots CD-3D, CD-4D and CD-Motion as a function of the number of denoising steps. Ours plateaus by step 4 on every metric, whereas ActionMesh keeps improving up to ~ 10 – 20 steps. On CD-3D and CD-4D the gap is large in the few-step regime that matters for inference cost: at 4 steps ours is roughly $2\times$ better on CD-3D (0.048 vs. 0.095) and CD-4D (0.077 vs. 0.125), and stays strictly better

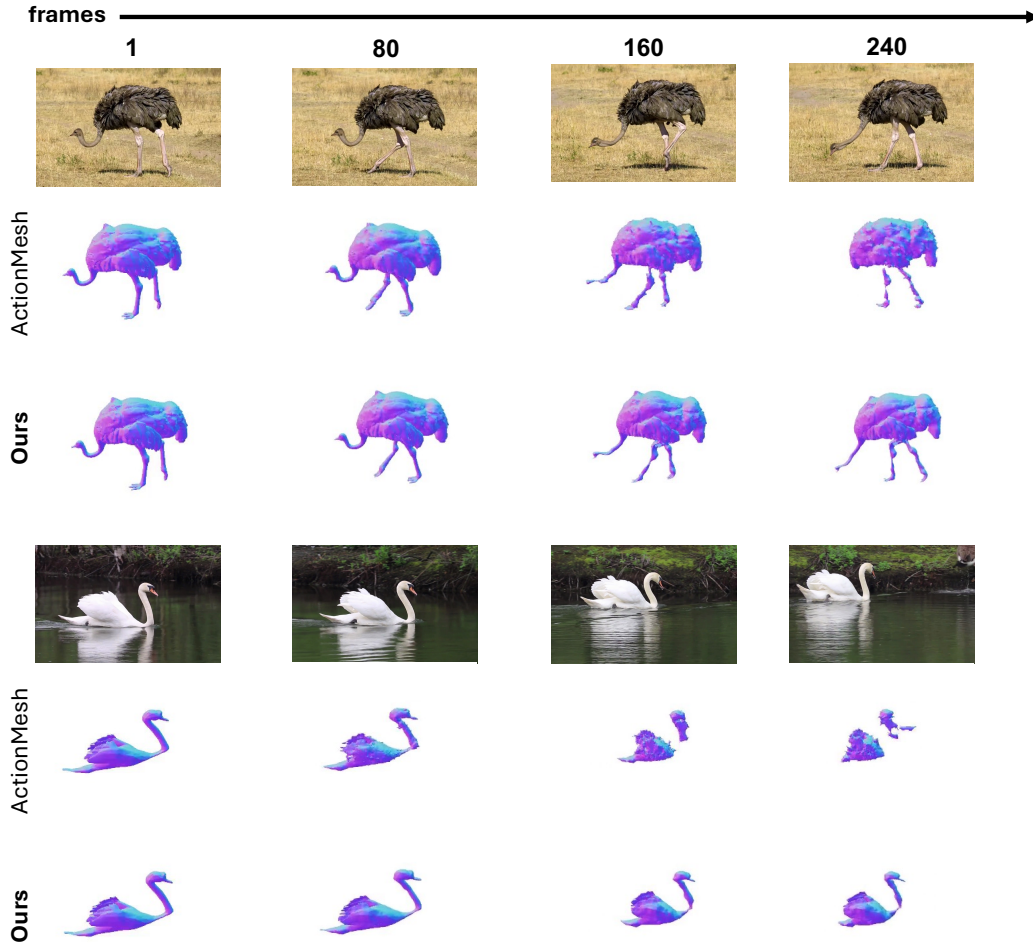


Figure 6: **Long-sequence autoregressive generation.** Mesh quality over 240 frames (sampled at frames 1, 80, 160, 240). ActionMesh progressively degrades due to accumulated drift across autoregressive windows, eventually losing recognizable geometry. Our correspondence reinforcement maintains stable, high-quality meshes throughout the entire sequence.



Figure 7: **Zero-shot 2D point tracking.** Comparison with Denoise-to-Track [92] on challenging sequences with articulated motion. Colored dots mark tracked query points; trails show predicted trajectories. Our attention-chain correspondences yield geometrically grounded tracks that more faithfully follow the underlying surface motion, particularly on limbs and fine structures.

even at 30 steps. On CD-Motion ActionMesh is consistently slightly better – its learned Stage II

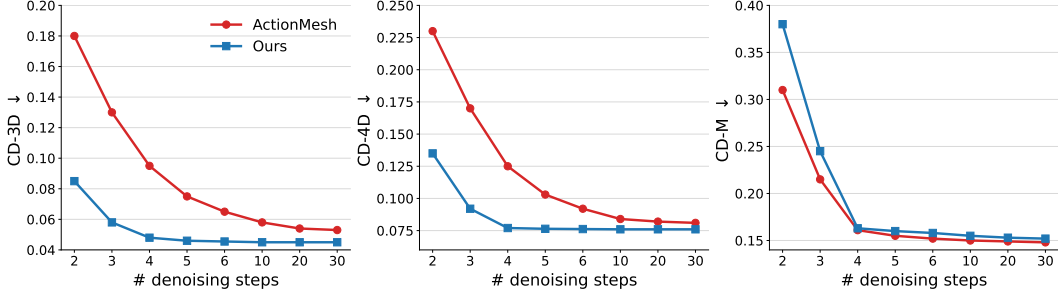


Figure 8: CD-3D / CD-4D / CD-Motion vs. Stage I denoising steps on ActionBench. Ours plateaus by step 4 and decisively wins CD-3D and CD-4D at every step count; ActionMesh’s learned Stage II is consistently smoother on CD-Motion.

yields smoother frame-to-frame motion than our closed-form correspondence chain (0.148 vs. 0.152 at 30 steps; 0.161 vs. 0.163 at 4 steps), with the gap growing at very few steps where Stage II is most needed to clean up noisy latents. The remaining headroom on motion smoothness is therefore in the temporal regulariser, not in the underlying correspondence. All other experiments use 5 denoising steps.

Inference time breakdown. We accelerate 4D mesh generation in two complementary ways (Table 3). **(i) Many fewer denoising steps.** Our correspondence is robust to slightly noisy latents and saturates by step 4 on every metric (Fig. 8), whereas ActionMesh requires ~ 30 steps for its Stage II network to operate at peak quality – shrinking Stage I from ~ 100 s to ~ 7.5 s on the same backbone. **(ii) No additional network.** We drop ActionMesh’s learned Stage II (~ 10 s) entirely and replace it with a lightweight, training-free pipeline of four closed-form operations: a single batched VAE decode for all frames at once (1.0 s), FPS landmark sampling on the anchor mesh (0.46 s), the $V \rightarrow T \rightarrow T \rightarrow V$ correspondence computation (0.16 s), and a geodesic, topology-preserving animation (0.8 s) – altogether ~ 2.4 s. End-to-end our full pipeline takes ~ 9 s per 16-frame clip, vs. ~ 110 s for ActionMesh: an order-of-magnitude speed-up without any loss of quality on CD-3D / CD-4D (Sec. 5.1).

Component contribution on long videos. Table 4 ablates the three components of our long-video pipeline on the 240-frame split of ActionBench, evaluated *without* ICP so that the metrics reflect the *intrinsic* alignment of each variant. ActionMesh in this regime is unaligned: its Stage II is trained on 16-frame clips and its autoregressive extension drifts in absolute pose, leading to large CD and motion errors. Replacing Stage II with our attention-chain correspondence (Sec. 4.1) tightens both metrics. Periodically re-encoding the anchor across windows (Sec. 4.3) further removes intra-AR drift. Finally, PnP-based camera-pose estimation (Sec. 4.4) folds out the remaining global rigid mismatch and gives the largest jump on CD-3D and CD-Motion. Our full pipeline more than halves both CD and motion error on the same backbone, *without* ICP.

C Implementation Details

Backbone and pipeline. We inherit the frozen, off-the-shelf two-stage backbone of ActionMesh [59]: Stage 0 is TripoSG [41], an image-to-3D diffusion model that produces the anchor mesh \mathcal{M}_a (~ 20 k vertices after decimation) and its latent code $z_a \in \mathbb{R}^{N \times d}$ with $N = 2048$, $d = 64$; Stage I is a flow-matching temporal denoiser Φ_θ that jointly produces per-frame latents $Z = \{z_f\}_{f=0}^{F-1}$ in a window of $F = 16$ frames, conditioned on per-frame DINOv2 [52] patch features and anchored at z_a . **We never train or fine-tune any model:** all weights are frozen, and our entire pipeline reduces to (i) reading the $V \rightarrow T$ cross-attention of the TripoSG VAE decoder and the inflated self-attention of Φ_θ at the first 3 denoising steps, and (ii) a sequence of closed-form correspondence and skinning operations (Sec. 4.1). The same attention chain serves 2D point tracking, 4D point tracking, and camera-pose estimation (Sec. 4.4). For 2D and 4D tracking under occlusions or unstable object masks, we first apply object an amodal completion using video diffusion model [48] before running our correspondence and deformation pipeline. For sequences longer than F frames we run a sliding 16-frame window with periodic anchor re-encoding (Sec. 4.3).

Table 3: Per-clip wall-clock breakdown (16 frames). Ours accelerates generation in two ways: (i) Stage I with 4 denoising steps instead of 30; (ii) replacement of ActionMesh’s learned Stage II network with a lightweight, training-free pipeline of four cheap closed-form operations. The two together reduce per-clip latency from ~ 110 s to ~ 9 s.

	ActionMesh [59]	Ours
Stage I (per-frame latents Z)	100.00 (<i>30 steps</i>)	7.50 (<i>4 steps</i>)
Stage II (per-frame meshes)	15.00 (<i>learned</i>)	1.49 (<i>training-free</i>)
batched VAE decode (all frames at once)	–	0.87
FPS landmarks (anchor mesh)	–	0.46
correspondence computation (attention chain)	–	0.16
geodesic topology-preserving animation	–	0.005
Total	110.00s	9.0s

Table 4: Component ablation on 240-frame sequences, *no ICP*. We start from ActionMesh’s unaligned predictions and add our components one-by-one. Lower is better.

Configuration	CD-3D ↓	CD-4D ↓	CD-M ↓
ActionMesh [59] (unaligned)	0.260	0.260	0.373
+ temporal correspondence (Sec. 4.1)	0.190	0.195	0.310
+ long-video AR (Sec. 4.3)	0.155	0.162	0.250
+ camera-pose estimation (Sec. 4.4)	0.108	0.115	0.198

Hyperparameters. After a coarse grid search we fixed a single configuration that we use across *every* experiment in this paper – 4D mesh generation, 2D and 4D point tracking, and the long-video stress tests – with no per-scene tuning. The values are: 4 Stage I denoising steps (justified in Fig. 8); 1000 FPS landmarks on the anchor mesh with curvature boost $\alpha = 2.0$; outlier rejection at $5\times$ the per-landmark median displacement and a $\geq 95\%$ valid-frame requirement; Gaussian smoothing of landmark displacements with $\sigma_{\text{landmark}} = 1.5$ and of the full vertex displacement field with $\sigma_{\text{final}} = 1.0$; a geodesic-rigid skinning with $k_{\text{NN}} = 120$ Dijkstra neighbours (auto σ).

For the camera intrinsics, we assume a fixed focal length of 2.1875 defined in canonical Normalized Device Coordinates (NDC). Because the NDC image extent spans $[-1, 1]$, this value is independent of pixel resolution and corresponds to a full vertical field-of-view of roughly 49.2° . Camera poses are then estimated using a robust PnP solver implemented as a RANSAC loop with EPnP as the minimal solver, an 8-pixel reprojection-error inlier threshold, 400 iterations at 0.999 confidence, an SQPnP consistent-solver fallback when EPnP returns a degenerate (near-camera-at-infinity) translation, and a final Levenberg–Marquardt refinement on the inlier set.

Synthetic Long Sequences In Section 4.3, we generate extended ActionBench [59] sequences by employing a *ping-pong* looping scheme. Because standard ActionBench sequences are limited to exactly 16 frames, we artificially lengthen the temporal duration of the videos by continuously playing the frames forward and then in reverse. Specifically, the sequence ordering follows the alternating pattern $(f_0, f_1, \dots, f_{14}, f_{15}, f_{14}, \dots, f_1, f_0, f_1, \dots)$. This progression allows us to generate arbitrarily long sequences while preserving smooth and continuous motion transitions.

D Topology-Preserving Animation Details

This section provides the mathematical details for the temporal smoothing and mesh deformation steps introduced in Section 4.2.

D.1 1D Gaussian Temporal Smoothing

The raw trajectories of the control landmarks, extracted from the attention chain, are denoted by $\tilde{\mathbf{v}}_\ell^{(f)}$ for landmark ℓ at frame f . To reject physically implausible predictions, we apply an outlier filtering step. Specifically, we flag a landmark’s displacement as an outlier if its magnitude exceeds a

relative threshold (e.g., $5\times$ the median displacement magnitude of all landmarks in that frame) or an absolute distance threshold. We assign a confidence score $c_\ell^{(f)}$ to each prediction, where $c_\ell^{(f)} = 0$ if the displacement is flagged as an outlier, and $c_\ell^{(f)} = 1$ otherwise.

To bridge the gaps caused by rejected outliers and ensure fluid motion, we apply a confidence-weighted 1D Gaussian temporal smoothing independently to each landmark’s trajectory. Crucially, we smooth the *displacements* from the anchor pose rather than the absolute positions. This ensures that stationary landmarks do not artificially drift over time.

The smoothed position $\hat{\mathbf{v}}_\ell^{(f)}$ for landmark ℓ at frame f is computed as:

$$\hat{\mathbf{v}}_\ell^{(f)} = \mathbf{v}_\ell^a + \frac{\sum_j G_\sigma(f, j) c_\ell^{(j)} (\hat{\mathbf{v}}_\ell^{(j)} - \mathbf{v}_\ell^a)}{\sum_j G_\sigma(f, j) c_\ell^{(j)} + \epsilon},$$

where \mathbf{v}_ℓ^a is the position of the landmark in the anchor mesh, $G_\sigma(f, j) = \exp\left(-\frac{(f-j)^2}{2\sigma^2}\right)$ is a 1D Gaussian kernel with standard deviation σ (in frames), and ϵ is a small constant for numerical stability. The anchor frame itself is pinned to its original geometry to prevent any smoothing leakage.

D.2 Local Rigid Deformation

To propagate the smoothed landmark motions to the dense mesh, we use a local rigid deformation formulation related to As-Rigid-As-Possible (ARAP) surface modeling [65]. Standard linear blend skinning interpolates displacement vectors, which famously causes volume loss when regions undergo rotation. By instead solving for a local rigid transformation (rotation and translation) for each vertex, we preserve the local volume of the mesh.

For each free vertex v on the anchor mesh, we identify its K_{nn} geodesically closest landmarks, denoted as the neighborhood \mathcal{N}_v . We assign a Gaussian weight to each landmark $\ell \in \mathcal{N}_v$ based on its geodesic distance $d_{v\ell}$ on the anchor mesh:

$$w_{v\ell} = \exp\left(-\frac{d_{v\ell}^2}{2\sigma_{geo}^2}\right),$$

where σ_{geo} is a scaling factor proportional to the mean spacing between landmarks. The weights are normalized such that $\sum_{\ell \in \mathcal{N}_v} w_{v\ell} = 1$. Using geodesic distances ensures that the deformation respects the surface topology and articulations (e.g., preventing a landmark on the torso from inappropriately influencing the arm).

For each frame f , we solve a weighted Procrustes alignment to find the optimal rotation $R_v^{(f)} \in SO(3)$ that maps the anchor landmark positions to their smoothed target positions:

$$R_v^{(f)} = \arg \min_{R \in SO(3)} \sum_{\ell \in \mathcal{N}_v} w_{v\ell} \left\| R(\mathbf{v}_\ell^a - \boldsymbol{\mu}_v^a) - (\hat{\mathbf{v}}_\ell^{(f)} - \boldsymbol{\mu}_v^{(f)}) \right\|_2^2,$$

where $\boldsymbol{\mu}_v^a$ and $\boldsymbol{\mu}_v^{(f)}$ are the weighted centroids of the neighborhood in the anchor and target frames, respectively:

$$\boldsymbol{\mu}_v^a = \sum_{\ell \in \mathcal{N}_v} w_{v\ell} \mathbf{v}_\ell^a, \quad \boldsymbol{\mu}_v^{(f)} = \sum_{\ell \in \mathcal{N}_v} w_{v\ell} \hat{\mathbf{v}}_\ell^{(f)}.$$

Once the optimal rotation $R_v^{(f)}$ is found via Singular Value Decomposition (SVD), we apply the rigid transformation to the vertex’s anchor position to obtain its final animated position:

$$\hat{\mathbf{v}}_v^{(f)} = R_v^{(f)} (\mathbf{v}_v^a - \boldsymbol{\mu}_v^a) + \boldsymbol{\mu}_v^{(f)}.$$

Applying this transformation to all vertices yields the final animated mesh $\hat{\mathcal{M}}_f = (\hat{\mathbf{V}}^{(f)}, \mathcal{F}_a)$.

D.3 User Study Details

To complement the geometric metrics reported in Sec. 5.1, we conducted a perceptual user study that directly compares our 4D mesh generation against ActionMesh [59], the strongest baseline in

this setting. We randomly sampled 20 clips for the study and for each clip, both methods were run with their default settings on the same input frames; the resulting 4D meshes were rendered from the input camera and assembled into a single side-by-side video that places the two renderings next to the reference input. Each trial shows this triplet to the rater, with the left/right ordering of the two methods randomised per trial to remove positional bias, and asks: “*Which result better matches the reference video in terms of appearance and motion consistency (i.e., fewer temporal mesh distortions)?*” The rater must pick exactly one of the two options. We recruited 100 independent raters, each judging all 20 clips, which yields 2,000 pairwise comparisons in total. Across this entire pool, 85% of the judgments favour our method, and the preference is consistent across clips and categories. This perceptual margin mirrors the quantitative findings of Tab. 1: our renderings exhibit sharper geometry, more accurate silhouette alignment with the input view, and noticeably fewer temporal jitters and mesh distortions than ActionMesh.